Application of percolation, critical-path, and effective-medium theories for calculation of two-phase relative permeability

Saurabh Naik,[1] Kirill M. Gerke,[2,*] Zhenjiang You,[3] and Pavel Bedrikovetsky[1]
[1]*Australian School of Petroleum and Energy Resources, The University of Adelaide, South Australia, SA 5005, Australia*
[2]*Schmidt Institute of Physics of the Earth of Russian Academy of Sciences, Moscow 123242, Russia*
[3]*School of Chemical Engineering, The University of Queensland, Brisbane Qld 4072, Australia*

(Received 13 January 2021; accepted 19 March 2021; published 22 April 2021)

There has been active development of numerical pore-network simulation of two-phase immiscible flows in porous media in recent years. These models allow for generation of capillary pressure and relative permeability curves. However, percolation models provide an efficient alternative, with reduced reliance on numerical techniques. Implementation of effective medium or critical path theory along with the percolation model allows for evaluation of the relative permeability curves. Both approximations failed to match the irreducible water saturation for water relative permeability. While the effective medium approximation poorly matches the pore network simulator, the critical path approximation is shown to match the result of the oil relative permeability. Despite the difference in end points, there is qualitative agreement between critical path approximation and the pore network simulator. Moreover, observed differences are not necessarily a drawback due to important boundary effects as discussed in the paper. Our results indicate that percolation-theory based predictions have the potential to become an efficient tool for upscaling by computing two-phase flow properties for numerous porosity subdomains.

DOI: 10.1103/PhysRevE.103.043306

I. INTRODUCTION

Prediction of the porous media flow properties is important in numerous disciplines, notable examples include hydrocarbon extraction [1,2] and the design of fluid injection programs for underground reservoirs [3,4]. While primary drainage occurs during geological secondary migration of hydrocarbons and CO_2 sequestration injection into aquifers, primary imbibition is important for water flooding of oilfields. The relative permeability curves play essential roles in parameterizing continuum media models and simulating large scale flow and transport phenomena.

In reservoirs which exhibit large changes in permeability or capillary pressure, the forms of the capillary pressure and relative permeability curves will have a strong impact on the performance of the extraction or injection program. Close to the wellbore, there can be a large reduction in capillary pressure. The saturation and pressure profiles close to the wellbore can be highly affected by the aforementioned curves.

Such curves will be influenced by the physical characteristics of the pore network, the surface of the solid walls and the interfacial properties of the two phases. To appropriately model the influence of interfacial tension reduction or contact angle alteration, so-called pore-scale modeling techniques are invaluable as, unlike laboratory measurement, they allow one to perform numerous experiments using the same digital pore structure model. The latter can be obtained using x-ray computed tomography (XCT) [5], stochastic reconstructions [6–11] or their superposition [12,13].

A variety of computational methods exist to simulate single and multiphase fluid flow within heterogeneous pore spaces. Among the most popular are the Lattice Boltzmann method [14,15]; (2) finite element, finite volume, and volume of fluid methods [16,17]; (3) smoothed particle hydrodynamics [18]; (4) finite-difference Stokes equation solvers [19,20]; (5) level set [17,21]; (6) phase-field [22,23] and density functional theory based [24] methods. While debates about the advantages and downsides of each approach are far from settling down, even with modern parallelized computations and hardware, all these methods are extremely computationally intensive. This limits the size of the simulation domain that can be evaluated to a limited volume of usually 300^3–700^3 voxels, while the time needed with high performance computing (HPC) resources easily reaches several weeks. For complex and hierarchical porous media, the problem is exacerbated due to the need to work on as large as possible three-dimensional (3D) pore geometries to capture the representative elementary volume (REV) of a porous medium or to work on fused 3D structure models resulting from a number of multiscale images for samples such as shales [25,26], carbonates [27] or soils [28]. We confidently conclude that such direct pore-scale modeling techniques are too computationally expensive to routinely process REVs of real rock samples.

To make pore-scale simulations for complex hierarchical porous media practical one can utilize indirect modeling methods such as pore-network models (PNMs) [29–33]. There have been classical pore-network simulation models developed in Refs. [34,35] which can calculate the relative permeability and capillary pressure curves accounting for wettability and interfacial tension effects in the quasistatic regime. While significantly reducing the complexity

*Corresponding author: kg@ifz.ru

of the simulations, PNMs can suffer minimal accuracy reductions if parameterized using abovementioned direct pore-scale simulations [36,37]. Although PNMs allow a very efficient computational framework to simulate single-, two- and even three-phase [38–40] flows, if one fuses macro and micro XCT scans with stochastic reconstructions [41,42] based on scanning electron microscopy (SEM) or focused ion beam (FIB)-SEM images it is easy to hit more than 10^{10} pore-network elements where even PNM simulations can get prohibitive.

Another alternative to simulate flow properties even faster than PNM would be percolation models. The critical parameters which are required to analytically evaluate the network properties in percolation models only depend on the lattice type and the dimension of the network. Given that we have a reasonable estimate of a lattice which represents natural porous media and that the critical parameters have already been evaluated, properties such as the percolation threshold, and infinite cluster strength can be evaluated analytically. This allows for an analytical evaluation of the capillary pressure curve, as shown in Refs. [43,44].

However, the calculation of relative permeability is more challenging. While there are analytical expressions for network conductance, they are for Bethe lattices [45], which are not representative of natural porous media. Reference [46] provided an analytical expression for relative permeability, assuming saturation as equal to site occupancy and applying the percolation expression for conductance. The analytical expressions for relative permeability of periodical lattices are based on the network approximation by so-called r chains [47–49]. However, the conductance calculated using the percolation expression does not account for variability and disorder in the bond conductance distribution. Natural porous media have a variety of pore throat sizes, and consequently a variety of values for conductance. A more complicated approach is required when bond conductance is disordered.

One approach for disordered media is effective medium theory (EMT). Reference [50] presents the numerical validation of the EMT and shows that it accurately describes the conductance of the bond percolation problem, except close to the percolation threshold. There have been numerous publications on the application of EMT theory for calculation of relative permeability. However, the application of effective medium theory has had varying degrees of success.

The authors of Ref. [51] apply EMT but replace bond occupation directly with saturation. Close to threshold they use the percolation expression instead of EMT to calculate relative permeability. They find percolation exponents by fitting to capillary pressure data. Under this approach, they achieve good results for 14 out of 21 of the laboratory samples. They discuss that the deviation can occur from neglecting corner and film flow. Reference [52] improved on this work by incorporating pore-solid interface roughness effects in the hydraulic conductance of bonds.

The aim of this paper is to build upon previous knowledge and improve percolation models to determine the efficacy of EMT for the calculation of the two-phase relative permeability curves. Bond percolation models previously developed have required some correction to the relationship bond radius shared with volume and conductance by some empirical term [43,45] in order to achieve realistic relative permeability curves. In order to properly account for the difference in pore body and pore throat distributions a more sophisticated percolation model is developed. Our potential long-term aim is to establish a framework based on percolation theory for modeling multiphase flow which will be compatible to pore-network models in terms of speed (and even faster) and accuracy. This paper, thus, serves as a proof of concept which shows that our model is close to the PNM model in both accuracy and computational efficacy.

A site-bond percolation model which can utilize the effective medium or critical path approximations is derived to describe two-phase immiscible flow. This allows us to account for variability in pore body and throat sizes, without creating empirical parameters. The SEM or FIB-SEM techniques can be used to generate pore network models and create distributions for pore bodies and pore throats. To mimic irregular pore throat with corner flow, the percolation model uses a triangular prism for the pore throat and a cube for the pore body. A similar approach has been applied in Ref. [53], but using only bond percolation. They found dissimilar results between network simulator models and percolation EMT models. Reference [54] suggests that critical path theory (CPT) may be superior for calculation of networks with highly disordered conductance distributions. For this reason CPT is included in this paper. An EMT-percolation and CPT-percolation model is compared against a sophisticated pore network simulator with identical pore network topology for verification of the EMT and CPT during drainage of water by oil.

This paper presents a fast and robust percolation theory-based model to simulate single and two-phase flow within porous media with known pore size distributions. The model is presented in Sec. II. The generation of the input functions for the percolation model is described in Sec. III. A pore network simulator is compared to the percolation effective medium approach and the percolation critical path approach. The network simulator is described in Sec. IV. The results of the comparison are presented in Sec. V. The discussion of the results is provided in Sec. VI. Finally, the conclusions of the paper are presented in Sec. VII.

II. PERCOLATION MODEL FOR OIL-WATER DRAINAGE

In this work two types of lattices have been used to represent the porous media; a simple cubic lattice with coordination number $Z = 6$ and a simple cubic lattice with half the bonds turned off, resulting in an average coordination number of $Z = 3$. The network is composed of sites. Each site center is separated by a distance l to the next adjacent site in each of the three dimensions of the Cartesian coordinate system. Each site is connected to the Z nearest sites by a bond. Each site represents a pore body and each bond represents a pore throat. The pore bodies are modeled as cubes and the pore throats as triangular capillaries. The porous medium is initially filled by water and is further submitted to primary drainage by oil. A visual representation of the network is given in Fig. 1.

The drainage process is capillary dominated. This means that for oil to enter a pore body or throat the capillary pressure must exceed the entry pressure for that body or throat. The calculation of the entry pressure is covered in Appendix A 1–

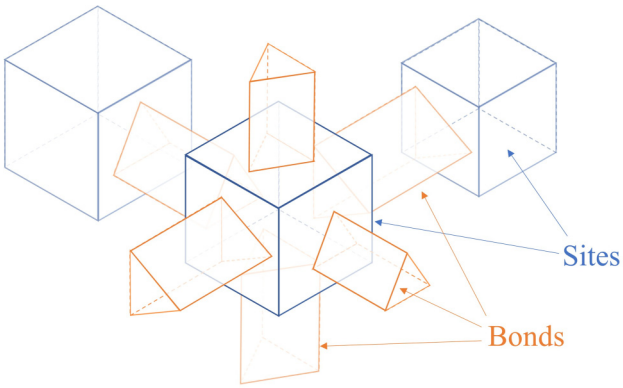

FIG. 1. Schematic of the percolation model.

A 3. The conductance of each bond or site to oil or water will also depend on the capillary pressure and how the oil or water phase distributes itself in the pore space. The calculation of conductance is covered in Appendix A 4. It is important to understand that capillary pressure alone is not the only factor which determines if a pore body or throat is penetrated by oil. In this paper, the bonds or sites where capillary entry pressure is exceeded will be referred to as "allowed" to be accessed by oil. The oil phase will enter through one face of the network. Any continuous chain of allowed sites and bonds which connect to this face of the network will become "occupied" by oil. The calculation of the proportion of occupied to allowed bonds and sites is covered in Sec. II A. Finally, given some proportion of the network is occupied by oil, the relative permeability to oil and water can be calculated. The technique using EMT is covered in Sec. II B and the technique using CPT is covered in Sec. II C.

A. Pore filling during drainage

The percolation model assumes that the inscribed radii of the sites are completely uncorrelated to the adjacent bonds. The frequency of bonds of inscribed radius r_{in} is defined by the function f_b. This means that the probability that any bond has inscribed radius greater than some r_1 and less than some r_2 is equal to the integral of f_b from r_1 to r_2. Similarly, the frequency of sites of inscribed radius r_{in} is defined by function f_s.

During drainage, the proportion of bonds available to be filled by oil p_{bo} can be calculated by

$$p_{\text{bo}} = \int_{r_b}^{r_{b\max}} f_b(r_{\text{in}})dr_{\text{in}}, \tag{1}$$

where r_b is the inscribed radius of the smallest bond available to oil and r_{bmax} is the inscribed radius of the largest bond. The inscribed radius is defined by

$$r_b = \frac{\sigma_{\text{ow}}}{P_c D_r}, \tag{2}$$

where P_c is capillary pressure, σ_{ow} is the interfacial tension between oil and water and D_r is a constant derived using Mayer-Stowe-Princep (MSP) theory. The derivation of this constant is covered in Appendix A. The proportion of sites available to be filled by oil p_{so} can be found from

$$p_{\text{so}} = \int_{r_s}^{r_{s\max}} f_s(r_{\text{in}})dr_{\text{in}}, \tag{3}$$

where r_s is the inscribed radius of the smallest site available to oil. It is defined by

$$r_s = \frac{2\sigma_{\text{ow}}}{P_c}. \tag{4}$$

The pore volume made up of sites ϕ_s is calculated by

$$\phi_s = \int_{r_{s\min}}^{r_{s\max}} f_s(r_{\text{ins}}) 8 {r_{\text{ins}}}^3 dr_{\text{ins}}, \tag{5}$$

where $r_{s\max}$ is the inscribed radius of the largest site. The volume of oil in the site V_{so} is approximated by

$$V_{\text{so}}(r_{\text{in}}, r_d) = 8{r_{\text{in}}}^3 - 24 r_{\text{in}} A_{\text{wc}}(\theta, r_d, \beta), \tag{6}$$

where r_d is the radius of curvature, A_{wc} is the cross-sectional area for corner water and β is the half angle of the corner. The calculation of A_{wc} is covered in Appendix A. This equation does not properly account for the water volumes in the corner. However, the same equation is used in the pore network simulator, which allows for the percolation model results to be compared with the pore network simulator.

The oil saturation in the sites s_{so} is calculated by

$$S_{\text{so}} = \frac{p_{s\infty}(p_{\text{so}}, p_{\text{bo}})}{p_{\text{so}}\phi_s} \int_{r_s}^{r_{s\max}} f_s(r_{\text{in}}) V_{\text{so}}(r_{\text{in}}, r_d) dr_{\text{in}}, \tag{7}$$

where $p_{s\infty}$ is the proportion of sites occupied by oil. The pore volume made up of bonds ϕ_b is calculated by

$$\phi_b = \frac{Z}{2} \int_{r_{s\min}}^{r_{s\max}} \int_{r_{s\min}}^{r_{s\max}} \int_{r_{b\min}}^{r_{b\max}} f_b(r_{\text{inb}}) f_s(r_{\text{ins1}}) f_s(r_{\text{ins2}}) \times A_b(r_{\text{inb}}) l_b(r_{\text{ins1}}, r_{\text{ins2}}) dr_{\text{inb}} dr_{\text{ins1}} dr_{\text{ins2}}, \tag{8}$$

where Z is the coordination number of the network, A_b is the cross-sectional area for the bond and l_b is the length of the bond. The oil saturation from bonds S_{bo} is calculated by

$$S_{\text{bo}} = \frac{p_{b\infty}(p_{\text{so}}, p_{\text{bo}})}{{p_{\text{so}}}^2 p_{\text{bo}}\phi_b} \int_{r_{s\min}}^{r_{s\max}} \int_{r_{s\min}}^{r_{s\max}} \int_{r_b}^{r_{b\max}} f_b(r_{\text{inb}}) f_s(r_{\text{ins1}}) \times f_b(r_{\text{ins2}}) A_{\text{bo}}(r_{\text{in}}, r_d, \theta) l_b(r_{\text{ins1}}, r_{\text{ins2}}) dr_{\text{inb}} dr_{\text{ins1}} dr_{\text{ins2}}, \tag{9}$$

where $p_{b\infty}$ is proportion of bonds occupied by oil and A_{bo} is the cross-sectional area for oil in the bond. The total water saturation S_w is then calculated by

$$S_w = 1 - (S_{\text{so}}\phi_s + S_{\text{bo}}\phi_b). \tag{10}$$

The calculation of A_b, A_{bo}, and l_b are covered in Appendix A. The functions $p_{b\infty}$ and $p_{s\infty}$ are calculated numerically using a code developed in-house in the numerical computing environment MATLAB®. The algorithm is outlined in Sec. III. The results of numerical calculation are presented in Fig. 2. As the network is calculated on a finite $40 \times 40 \times 40$ grid, there are nonzero values of $p_{b\infty}$ and $p_{s\infty}$ before the percolation threshold.

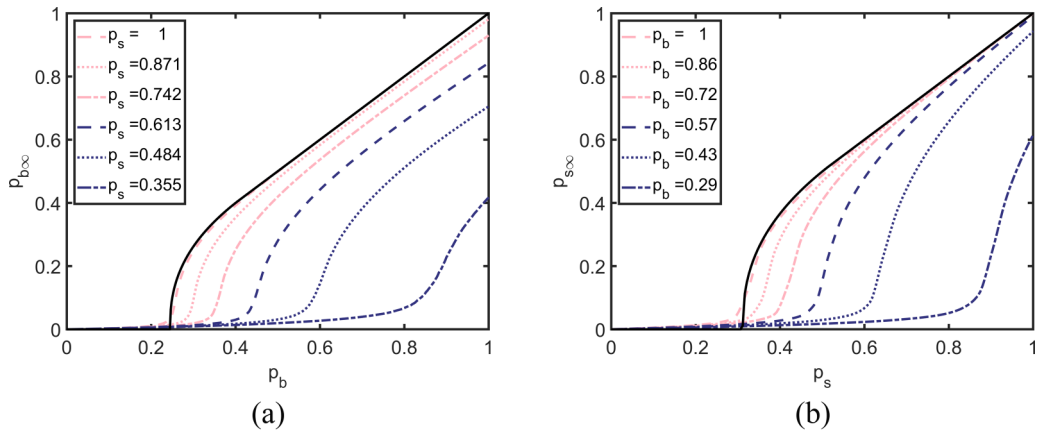

FIG. 2. Numerical calculation of the infinite cluster strength during the site-bond percolation process on a simple cubic lattice during bond (a) or site (b) percolation. In (a) bonds are forming an infinite cluster ($p_{b\infty}$) against available bonds (p_b) for different proportion of available sites (p_s) compared to the analytical model (in black) during bond percolation. In (b) sites are forming an infinite cluster ($p_{s\infty}$) against available sites for different proportion of available bonds compared to the analytical model (in black) during site percolation.

B. Effective medium theory

EMT is used to approximate the conductance of a network. It approximates a network with some distribution of bond conductance g_p with an equivalently conductive network where each bond conductance is equal to the effective medium conductance g_e. It is also called the effective medium approximation (EMA). Reference [50] derived the equation of effective conductance as

$$\int_0^\infty h(g_p)\frac{g_p - g_e}{g_p + \left(\frac{Z}{2} - 1\right)g_e}dg_p = 0, \tag{11}$$

where h is the frequency of conductance g_p in the network, and Z is the coordination number. Given our distribution of bond sizes and site sizes, Monte Carlo simulation can be used to quickly obtain the conductance distribution. In total 2×10^6 Monte Carlo permutations are used for generation of the conductance distributions. In this paper we use the coefficient of variation (c_v) to show convergence of the Monte Carlo simulation. The coefficient of variation is a widely used statistical measure of the dispersion of data points in a data series around the mean of the data series. It is the ratio of the standard deviation to the mean. Figure 14 in Appendix B shows the convergence of the permeability calculation. The probability of a site or bond can be found from the site or bond size distribution, respectively.

The distribution for oil can be generated, by assigning all sites smaller than r_s and all bonds smaller than r_b to have no oil conductance. The probability distribution used for the Monte Carlo simulation is

$$P(r_{\text{ins}}) = \begin{cases} 0 & , r_{\text{ins}} < r_s \\ f_s(r_{\text{ins}})/p_s & , r_{\text{ins}} > r_s \end{cases},$$
$$P(r_{\text{inb}}) = \begin{cases} 0 & , r_{\text{inb}} < r_b \\ f_b(r_{\text{inb}})/p_b & , r_{\text{inb}} > r_b \end{cases}. \tag{12}$$

The conductance to oil from one site to the next, g_o, is calculated in the following equation:

$$\frac{l}{g_o} = \frac{r_{\text{ins1}}}{g_{\text{os}}(r_{\text{ins1}})} + \frac{l_b}{g_{\text{ob}}(r_{\text{inb}})} + \frac{r_{\text{ins2}}}{g_{\text{os}}(r_{\text{ins2}})}, \tag{13}$$

where g_{os} is conductance to oil in the site and g_{ob} is conductance to oil in the bond. The subscripts 1 and 2 define the first and second site, respectively. The integral of the distribution of oil conductance h_o, should be equal to the number of bonds available to oil. Therefore, the normalized distribution generated by the Monte Carlo simulation is multiplied by p_b to get the conductance distribution h_o. Finally, the conductance to oil can be calculated by solving the following equation for g_e:

$$\frac{-(1 - p_b)}{\left(\frac{Z}{2} - 1\right)} + \int_0^\infty h_o(g_o)\frac{g_o - g_e}{g_o + \left(\frac{Z}{2} - 1\right)g_e}dg_o = 0. \tag{14}$$

The EMA for water is more complex. There are six possible configurations that can exist between two sites and a bond. The diagram for each configuration is given in Fig. 3. C_1 to C_3 are configurations with oil in the bond. C_1 is the configuration with oil in both sites, C_2 is the configuration with oil in one

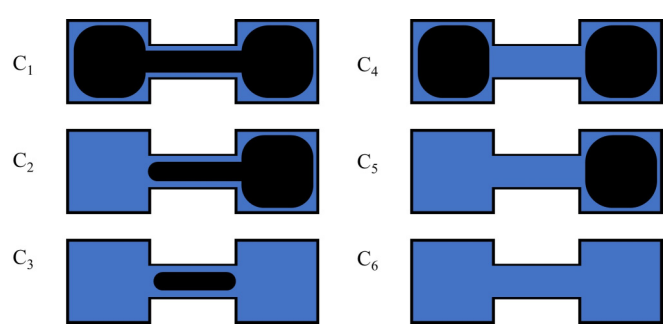

FIG. 3. The six configurations (C_1 to C_6) of oil and water which can exist in a bond and its two adjacent sites. The two squares represent the two sites and the rectangle in between represents the bond. The black color represents oil and the blue color represents water.

site and C_3 is the configuration with oil in no sites. Given that our problem considers capillary dominated drainage, the configuration C_3 will not exist. Henceforth it is ignored in the paper. The configurations C_4 to C_6 are configurations with water in the bond. C_4 is the configuration with oil in both sites, C_5 is the configuration with oil in one site, and C_6 is the configuration with oil in no sites. The conductance to water for configurations C_1 to C_6 are g_{w1} to g_{w6}. They are calculated by

$$\frac{l}{g_{w1}} = \frac{r_{\text{ins1}}}{g_{\text{wcs}}} + \frac{l_b}{g_{\text{wcb}}} + \frac{r_{\text{ins2}}}{g_{\text{wcs}}}, \tag{15}$$

$$\frac{l}{g_{w2}} = \frac{r_{\text{ins1}}}{g_s(r_{\text{ins1}})} + \frac{l_b}{g_{\text{wcb}}} + \frac{r_{\text{ins2}}}{g_{\text{wcs}}}, \tag{16}$$

$$\frac{l}{g_{w4}} = \frac{r_{\text{ins1}}}{g_{\text{wcs}}} + \frac{l_b}{g_b(r_{\text{inb}})} + \frac{r_{\text{ins2}}}{g_{\text{wcs}}}, \tag{17}$$

$$\frac{l}{g_{w5}} = \frac{r_{\text{ins1}}}{g_s(r_{\text{ins1}})} + \frac{l_b}{g_b(r_{\text{inb}})} + \frac{r_{\text{ins2}}}{g_{\text{wcs}}}, \tag{18}$$

$$\frac{l}{g_{w6}} = \frac{r_{\text{ins1}}}{g_s(r_{\text{ins1}})} + \frac{l_b}{g_b(r_{\text{inb}})} + \frac{r_{\text{ins2}}}{g_s(r_{\text{ins2}})}, \tag{19}$$

where g_{wcs} is the conductance in a site to corner water, g_{wcb} is the conductance in a bond to corner water, g_b is the conductance of a bond, and g_s is the conductance of a site. The probability that a bond or site with inscribed radius r_{inb} or r_{ins} has oil in the center is given by Eq. (12). The probability distribution that a bond or site with inscribed radius r_{inb} or r_{ins} only contains water is given by

$$P(r_{\text{ins}}) = \begin{cases} f_s(r_{\text{ins}})/(1-p_s) & , r_{\text{ins}} < r_s \\ 0 & , r_{\text{ins}} > r_s \end{cases},$$
$$P(r_{\text{inb}}) = \begin{cases} f_b(r_{\text{ins}})/(1-p_b) & , r_{\text{inb}} < r_b \\ 0 & , r_{\text{inb}} > r_b \end{cases}. \tag{20}$$

Given these probability distributions, the distribution of conductance made up by each of the configurations h_{wi} can be calculated using Monte Carlo simulation. The probabilities of configurations 1 to 6 are $p_1 \ldots p_6$. The probabilities depend on the proportion of sites and bonds available to the invading phase. They are calculated numerically using code developed in house in numerical computing environment MATLAB®. The results are given in Fig. 4. The total distribution for water conductance, h_w can be calculated by

$$h_w(g_w) = \sum_{i=1}^{i=6} p_i h_{wi}(g_{wi}). \tag{21}$$

Given the distribution for conductance to water, g_w, the effective conductance to water for the network is calculated by solving the following equation for g_e:

$$\int_0^\infty h_w(g_w) \frac{g_w - g_e}{g_w + \left(\frac{Z}{2} - 1\right) g_e} dg_o = 0. \tag{22}$$

The calculation of parameters g_w, g_o, g_b, g_s, g_{wcb}, and g_{wcs} is covered in Appendix A.

C. Critical path theory

A method of estimating the conductance of a disordered network was developed in Ref. [55]. The conductance of a set of parallel conductors is controlled by the largest conductor. The conductance of a set of conductors in series is controlled by the smallest conductor. They divide the network into two sets of conductors; small and large conductors. The smallest conductor of the large set is called the critical conductance g_c. All conductors greater than g_c are reduced to g_c and all conductors smaller than g_c are set to zero. The CPT shows that the resultant equation for conductance as given in Ref. [56] is

$$g_e = c_{\text{cpt}} g_c (p_{\text{cpt}}(g_c) - p_{\text{bth}})^\mu, \tag{23}$$

where c_{cpt} is a constant, μ is the percolation exponent for conductance (Ref. [56] gives a value of $\mu = 2$ for 3D networks) and p_{bth} is the bond percolation threshold. The probability p_{cpt} is the probability that a bond conductance is greater than or equal to some critical conductance g_c:

$$p_{\text{cpt}}(g_c) = \int_{g_c}^\infty h(g) dg. \tag{24}$$

The correct critical conductance g_c to use is the conductance which maximizes g_e [56]. To calculate the correct threshold to use during bond-site percolation, we will need the thresholds for site and bond percolation. The percolation threshold for bond percolation and site percolation in a simple cubic lattice is $p^*{}_{\text{bth}} = 0.2488$ and $p^*{}_{\text{sth}} = 0.3116$ [57], and this will be used throughout the paper. However, in the discussion section results for networks with various coordination numbers are required. For that section, the following expression for percolation thresholds of kagome lattices [57] is used:

$$p^*_{\text{th}} = \Upsilon_0 [(d-1)(Z-1)]^{-a_1} d^{a_2}, \tag{25}$$

where for sites $\gamma_0 = 1.2868$, $a_1 = 0.6160$, and $a_2 = 0$ and for bonds $\gamma_0 = 0.7541$, $a_1 = 0.9346$, and $a_2 = a_1$. The expression gives slightly different results for the percolation threshold of cubic lattice ($p^*{}_{\text{bth}} = 0.2448$ and $p^*{}_{\text{sth}} = 0.3115$), but the difference is only around 1.6% for bond percolation.

The percolation threshold for bonds in a bond-site network, p_{bth}, is dependent on the proportion of sites that can also contribute to the infinite cluster $p_{s\infty}$. Reference [58] obtained the following expression for the bond percolation threshold during bond-site percolation:

$$p_{\text{bth}}(p_{s\infty}) = (p^*_{\text{bth}})^{(1-\alpha_s(p_{s\infty}))}, \tag{26}$$

where

$$\alpha_s(p_{s\infty}) = \frac{\log(p_{s\infty})}{\log(p^*_{\text{sth}})}. \tag{27}$$

III. CALCULATION OF THE INFINITE CLUSTER AND CONFIGURATION PROPORTION DURING BOND-SITE PERCOLATION

The in-house code in Matlab® is developed for calculation of the percolation process across a $40 \times 40 \times 40$ simple cubic lattice. The cubic lattice with half of its bonds disabled and $p_b = 1$ will be equivalent to the cubic lattice when $p_b = 0.5$. For this reason, numerical calculation of the second lattic is not required. The procedure is as follows:

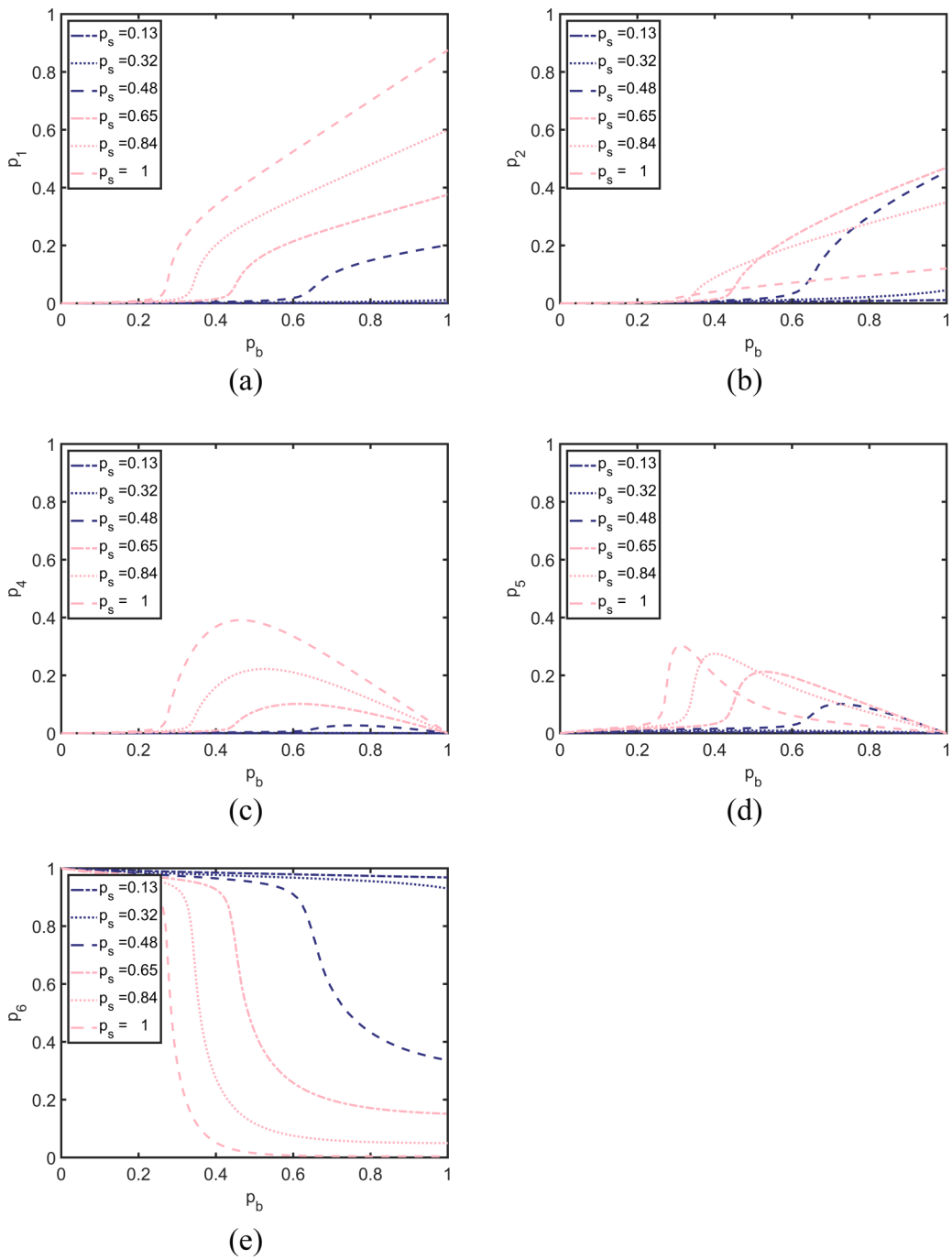

FIG. 4. Numerical calculation of the proportion of bonds which make up configurations C_1 to C_6 for various values of bonds (p_b) and sites (p_s) allowed to be penetrated by oil: (a) C_1; (b) C_2; (c) C_4; (d) C_5; (e) C_6.

(1) One face of the lattice network is designated as the entry for the invaded phase.

(2) Every bond and site is initially unavailable to the invading phase, meaning that $p_b = 0$ and $p_s = 0$.

(3) A proportion of sites is made available to the invading phase.

(4) One random bond in the lattice is made available to the invading phase.

(5) The proportions $p_{b\infty}$, $p_{s\infty}$, and p_1 to p_6 are calculated.

(6) Steps 4 to 5 are repeated until all the bonds are available to the invading phase.

The proportions $p_{b\infty}$, $p_{s\infty}$ and p_1 to p_6 are calculated for 120 simulations for 32 different values of p_s. Figures 2 and 4 show the average result of these simulations.

The calculation of $p_{b\infty}$ is given in Fig. 2(a). When all the sites are available, the infinite cluster strength for bonds follows the bond percolation process. As the proportion of available sites is reduced, $p_{b\infty}$ decreases. When the proportion of available sites drops below the site percolation threshold, the invading cluster can no longer form an infinite cluster.

The calculation of $p_{s\infty}$ is given in Fig. 2(b). Similar to the previous figure, the proportion of sites in the infinite cluster

will decrease as the number of bonds decrease. However, one difference is that if $p_b > 0.64$, all sites can be connected to the infinite cluster. If $p_b < 0.64$, there will be some proportion of sites which will be separate from the infinite cluster. This proportion will decrease as p_b decreases, and drop to zero once p_b is below the bond percolation threshold.

The probability of configuration C_1 will always monotonically increase as the number of bonds and sites available to be filled by oil increases [Fig. 4(a)]. When all the sites are available to oil ($p_s = 1$), the probability p_1 is the same as the infinite cluster strength during bond percolation. The probability of configuration p_2 will monotonically increase as the number of bonds to be filled by oil increases [Fig. 4(b)]. There exists some maximum for p_2 at some intermediate value for p_s. If there are no sites available to oil or if all the sites are available to oil, configuration C_2 cannot exist. Configuration C_2 only exists at some intermediate value for p_s.

The probabilities p_4 and p_5 share a nonmonotonic relationship with p_b [Figs. 4(c) and 4(d)]. If p_b is too low, not enough sites will become part of the infinite cluster. Otherwise, if p_b is too high, there will be less bonds occupied by the wetting phase. Proportion p_6 will monotonically decrease with increase in either p_b or p_s [Fig. 4(e)].

IV. PORE NETWORK SIMULATOR

As the target of all pore network simulations is a direct comparison against solutions obtained based on percolation theory, all physics mechanisms and parameters of the pore network simulator (PNS) are tuned to be the same as the percolation model.

At first, we constructed a lattice-based pore-network model with prescribed pore-body and pore-throat size distributions. Given the distance in between the pore bodies, we place them at the nodes of the lattice by randomly sampling from the size distribution. Next, we loop through each of the pore bodies and pore throat and assign the radii from the prescribed distribution. For the case where $Z = 3$, the number of throats attached to the given pore body is randomized. While placing throats we also perform body-throat partitioning that will define local element's conductance according to Eqs. (15)–(19). The length of throat is defined as in Eq. (13). The shape factors for all pore bodies and pore throats are assigned to equal that of the square and the equilateral triangle, respectively. The construction procedure as described above ensures that resulting characteristics of the constructed network are the same as those for percolation theory simulations [and no correlations exist between pore and throat placement as assumed in all percolation model (PM) computations] and for PNS on lattices with more than 10^3 throats the differences for pore, throat, length, and Z distributions are virtually negligible. This is observable in the comparison of the distributions used for the PM and the histogram of the elements for the PNS in Fig. 5.

After construction the pore network is saved into the so-called Statoil format and is also visualized using the open-source VTK library. All processing is performed using the in-house C++ code imbedded within the credible pore-network extraction framework [36,59] and the size of all models was 40^3 lattice units (totaling to 64×10^3 pore bodies

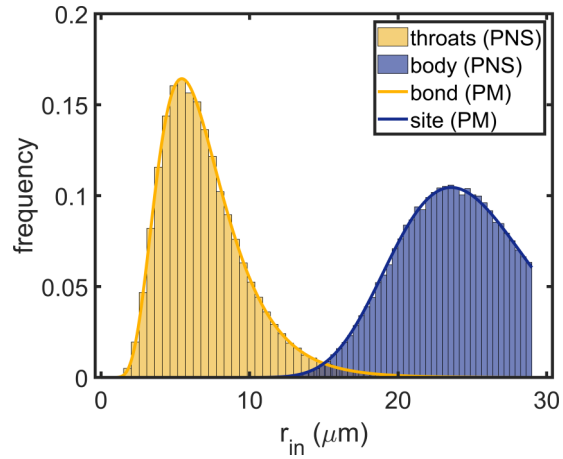

FIG. 5. Comparison of the site/bond size distributions used in percolation model (PM) against the throat/body distributions used in pore network simulator (PNS).

and 19.2×10^4 pore throats for $Z = 6$). The examples of visualizations for PNS with $Z = 6$ is presented in Fig. 6(a) and for $Z = 3$ in Fig. 6(b). For single and two-phase flow simulations the constructed pore network is passed into Valvatne's code [35], which utilized the same physics as described for PM. The flow was simulated in a single direction along one of major orthogonal axes. The contact angles within the network are assigned to $0°$ to represent fully water-wet conditions. The fluid properties for simulations using both theoretical and modeling approaches were chosen to represent a typical water-oil system with the surface tension of 30 mN/m. The only major difference between PM and PNS simulations lies with boundary conditions–with PNM simulator we utilized closed walls [60] on the faces of the cubical modeling domains parallel to applied pressure gradient. The simulated network permeability, capillary curves, and relative permeability curves for drainage from a network initially saturated with water were saved for comparison against PM results.

V. COMPARISON BETWEEN PERCOLATION MODEL AND PORE- NETWORK SIMULATOR

The PM developed in Sec. II is compared against the PNS described in Sec. IV. Four different distributions for bond

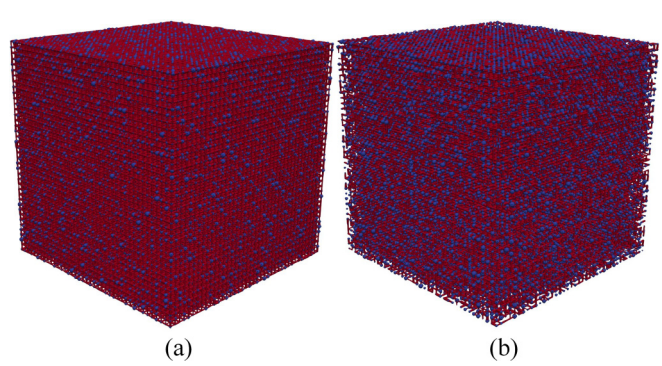

FIG. 6. Visualization of the pore network used in the pore network simulator: (a) $Z = 6$; (b) $Z = 3$.

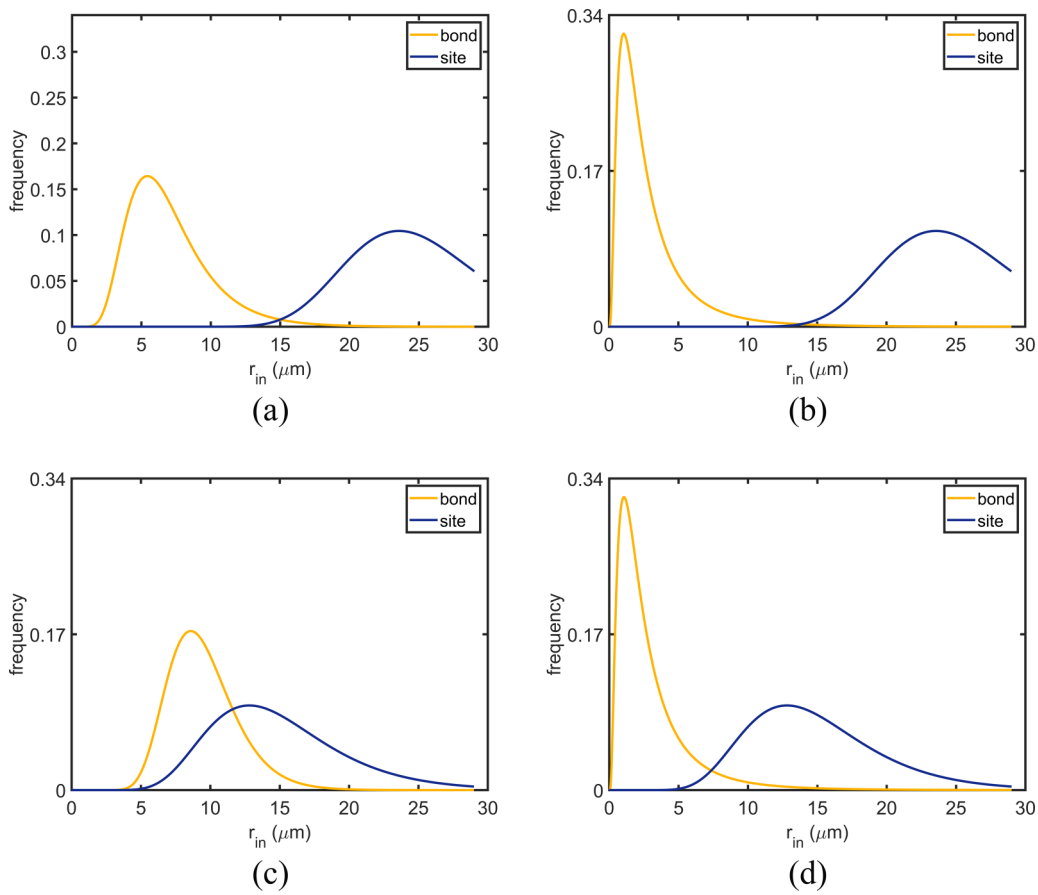

FIG. 7. Frequency of bonds and sites with inscribed radius r_{in} for: (a) distribution A; (b) distribution B; (c) distribution C; (d) distribution D.

inscribed radius and site inscribed radius were used. The probability density function for each of the site-bond distributions is shown in Fig. 7. The density functions are normalized lognormal distributions with an upper limit of 29 μm. The distance between adjacent sites is $l = 60\,\mu$m. In total 8 cases are compared.

The capillary pressure curves obtained from the percolation model show very high agreement with those from the PNS for all eight cases (Fig. 8). However, there is deviation in relative-permeability curves.

Figure 9 shows the comparison of pore network simulator with the percolation model with EMT and CPT for calculation of relative permeability for lattice with $Z = 6$. Figure 10 shows the same comparison but for the second lattice, where $Z = 3$. In all the cases, EMT deviates from the PNS.

Water relative permeability matches at very high water saturations but the pore network simulator diverges from the convex trend at lower water saturations. Generally, the PNS predicts higher water relative permeability. The CPT and EMT calculations for water relative permeability are similar. Both EMT and CPT can be treating the oil clusters as if they are randomly distributed throughout the network as opposed to a penetrating backbone cluster with many branches. They can therefore predict that more water pathways are broken than what is actually occurring. CPT predicts slightly lower water relative permeability to EMT in some cases. This is due to one of the assumptions associated with CPT. It assumes that the conductance for a set of conductors is in series and the overall conductance is equal to the smallest conductor in that set. The set is made up of a distribution of conductance, and if that set has a wide distribution this assumption can be accurate. But if that distribution has low variance, the assumption will under predict the overall conductance.

The oil relative permeability curve modeled by CPT matches the PNS much more closely than the other models. The reason could be that the penetrating cluster of oil could be bottlenecked by the smallest conductors in the set, which is more suitably calculated by CPT. The oil relative permeability curve modeled by EMT usually always terminates at lower water saturation than the pore network simulator. This is not uncommon, EMT has been reported in literature to underestimate permeability close to the threshold.

VI. DISCUSSION

One of the advantages of the EMT or CPT technique over the PNS is that it calculates over an infinite domain, whereas the PNS simulation works over a finite volume and must account for boundary conditions on the network. The impact of finite scale and boundaries can cause differences between the CPT, EMT, and PNS results [60].

The end point values for relative permeability; connate water saturation, residual oil saturation, water relative permeability at residual oil, and oil relative permeability at connate

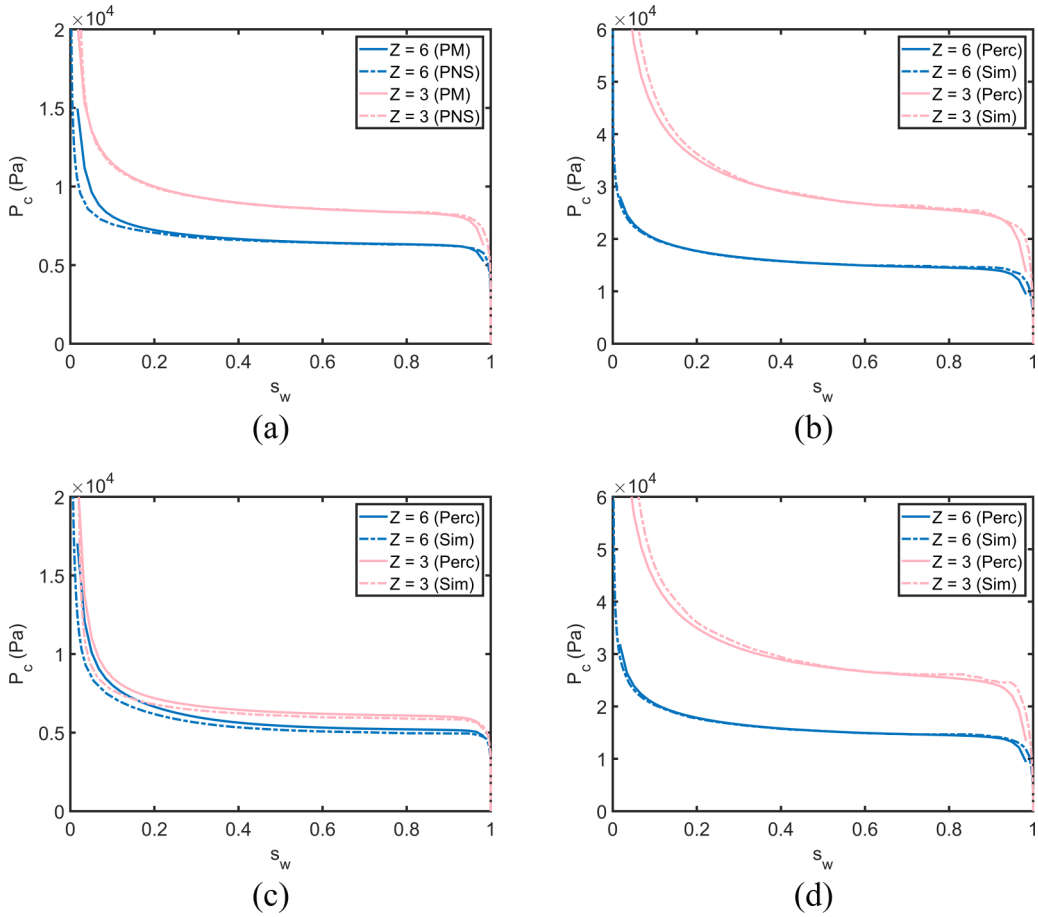

FIG. 8. A comparison between the capillary pressures calculated via the pore network simulator (PNS) and via the percolation model (PM) at coordination number (Z) 3 and 6: (a) distribution A; (b) distribution B; (c) distribution C; (d) distribution D.

water saturation are important parameters for calculation of water flood efficiency. The comparison shows large deviation using either EMT or CPT for the prediction of the relative permeability end points for all cases except for s_{or} at $Z = 6$. The $Z = 3$ will have a higher percolation threshold, for this reason EMT can be diverging from results of CPT and the PNS. However, the differences in predicted two-phase properties between PM and PNS are similar to the differences in different pore-network extraction methodologies [59].

The relative permeability calculated by the PNS has an inflection, and the relative permeability at any saturation lower than this inflection is higher for the PNS than the EMT or CPT models. The CPT and EMT methods will give permeability values close to zero as the probability of bonds occupied by water in the center tends to threshold, whereas in a finite model there can be instances of breakthrough before percolation threshold is reached. The pore network simulator could be calculating higher water relative permeability due to the finite size of the network. Simulations with pore networks of sizes up to 70^3 pores showed only marginal improvements in agreement with CPT results (and, thus, not shown here).

Pore-network simulators can be classified into two types: quasistatic and dynamic PNS. Our percolation theory based solution and PNS simulator both fall into the quasistatic category. While dynamic simulators do account for a richer variety of flow regimes (e.g., viscous fingering), they are much more computationally expensive [61]. On the other hand, by considering only capillary dominated flow, quasistatic models not only provide faster computations, but also align naturally with invasion percolation principles, as is exploited in EMT and CPT based simulations here and in previous work [43–46,49,51–56]. In addition to simplicity, one can argue that the quasistatic approach is valid for the majority of slow displacement processed during hydrocarbon production [2], and such PNS models were verified experimentally using computed tomography [62].

The percolation model predicts that water becomes immobile at saturation less than 0.5 for cases where $Z = 6$ and 0.7 for the cases where $Z = 3$. The relative permeability calculated by the percolation model shows either very small or almost no window of two-phase flow for the networks with $Z = 6$. For the networks with $Z = 3$, the percolation model calculates no window of saturation where both phases are mobile. The values of end point saturation and two-phase flow windows are unrealistic compared to natural porous media. The reason for these high values is that the percolation threshold is high.

For more realistic two-phase saturation windows and end point values, one option is to use higher coordination numbers. There are analytical expressions already available for

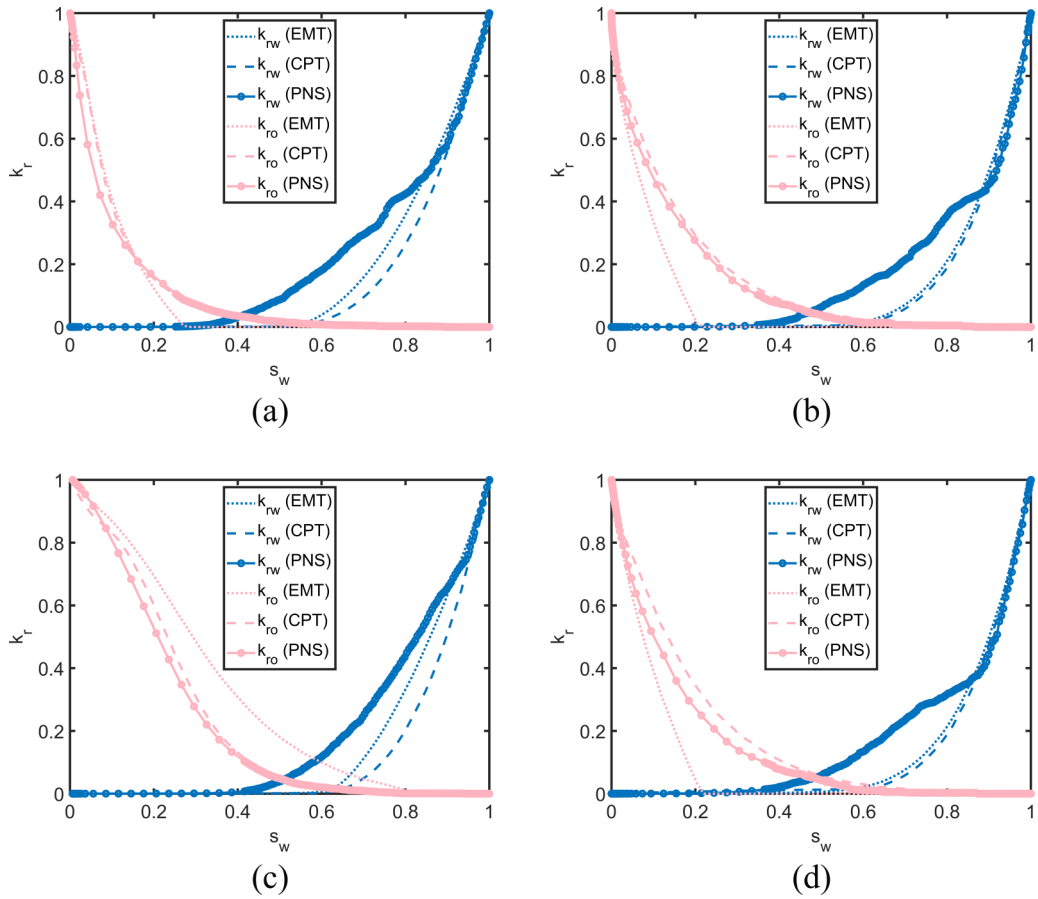

FIG. 9. A comparison between the relative permeability curves calculated via the pore network simulator (PNS) and via the bond-site percolation model with effective medium theory (EMT) and critical path theory (CPT), with an average network coordination number $Z = 6$: (a) distribution A; (b) distribution B; (c) distribution C; (d) distribution D.

percolation threshold in Ref. [57] and infinite cluster strength in Refs. [47,48] for bond percolation, so for this reason we investigate the end point value dependence on coordination number using just bond percolation. The end point values are determined from where the relative permeability calculated by CPT become 1×10^{-3}.

End point saturation values are given in Fig. 11(a) for Z-values from 3 to 12 and for three different values of coefficient of variation (c_v) in inscribed bond radius. The irreducible water saturation s_{wc} and the residual oil saturation s_{or} reduce as Z increases dues to the reduction in percolation threshold.

Increases in c_v cause an increase in the tail end of the lognormal distribution. As the area of the bond will scale to the power of 2 with the inscribed radius, the oil saturation will increase more than the water saturation when there is an increase in c_v. For this reason, an increase in c_v results in a decrease in s_{wc} and an increase in s_{or}. s_{wc} is more sensitive to c_v and Z than s_{or}. This is due to the distribution of smaller bonds being more affected by changes in c_v in a lognormal distribution.

The end point relative permeability values are shown in Fig. 11(b). The relative permeability to water at residual oil saturation k_{rwor} and the relative permeability to oil at irreducible water saturation k_{rowc} both increase as Z increases because the percolation threshold decreases. The conductance of the bond will scale to the power of 4 with the inscribed radius, so an increase in c_v will cause a dramatic increase in k_{rowc}. The window for two phase flow is presented in Fig. 12. As there is a decrease in both end point saturations with Z, the window will increase with Z.

However, the coordination numbers observed in sandstones are not on average that much higher than 6. Reference [63] calculates the average coordination number for several sandstones in the range 1.75 to 6.75. As the coordination number and pore body and throat size distributions should be input data for the percolation model, the avenue for improvement does not lie with modifying these parameters.

In some natural porous media, the larger pore bodies will have larger pore throats. This would cause the network to have correlation between available sites and bonds. There has been work done to find percolation thresholds and capillary pressure [64,65] in correlated site-bond percolation models, but none yet on relative permeability. Correlated bond-site percolation networks give lower thresholds, which can give relative permeability curves that are more representative of natural porous media. Additionally, the EMT technique, which is shown to be quite unsuccessful here, could be more reliable in networks with lower thresholds.

Moreover, direct simulations of percolation on pore networks extracted from 3D pore geometries of real porous

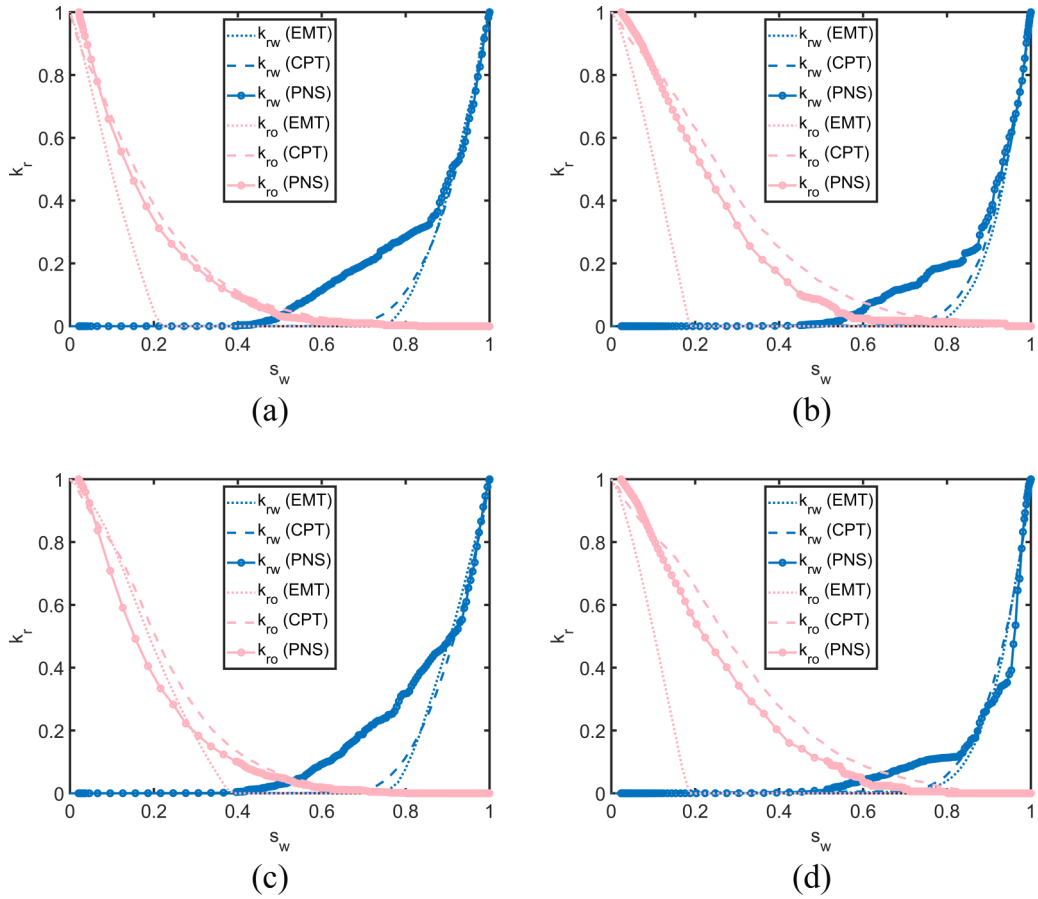

FIG. 10. Comparison between the relative permeability curves calculated via the pore network simulator (PNS) and via the bond-site percolation model with effective medium theory (EMT) and critical path theory (CPT), with an average network coordination number $Z = 3$: (a) distribution A; (b) distribution B; (c) distribution C; (d) distribution D.

media can serve as a much more accurate basis for percolation theory based models as discussed here. This should rely on future improvements of pore-network extraction methodologies, as the current methods are known to result in poor preservation of pore topology [66]. These shortcomings are not relevant to this study, as we compared artificially created networks which were not extracted from real 3D pore images.

While the comparison against PNS was made on the assumption that it provides a solid base for verification, it is possible to speculate that PM actually provides more accurate results. It was recently shown that boundary conditions can

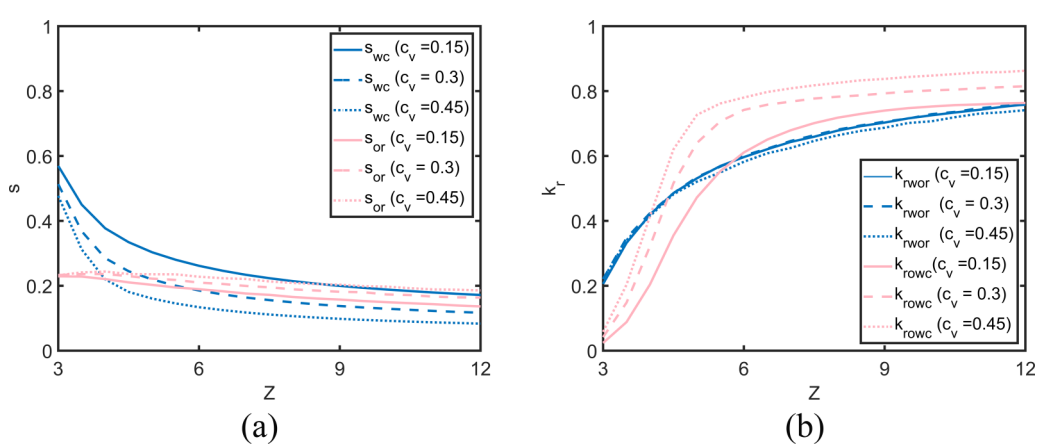

FIG. 11. Sensitivity of the end point values to coordination number as calculated by bond percolation and critical path theory for different coefficients of variation (c_v) in bond inscribed radius: (a) connate water saturation (s_{wc}) and residual oil saturation (s_{or}); (b) relative permeability to water at residual oil (k_{rwor}) and relative permeability to oil at connate water (k_{rowc}).

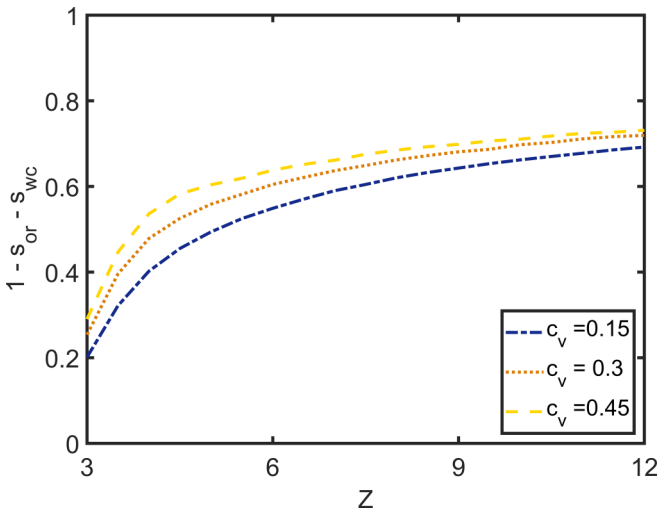

FIG. 12. The window of saturation where two phase flow exists as calculated by bond percolation and critical path theory. Sensitivity to the coordination number and the coefficient of variation for the bond radii.

significantly affect obtained flow properties [60] and closed walls boundary conditions on the walls of the modeling domain, as utilized in PNS, may not be appropriate for upscaling. Contrary to PNS, PM assumes infinite porous media domain, which is arguably a more plausible assumption for homogenization to continuum scale, as for example, is needed for multiscale PNS [27].

VII. CONCLUSIONS

This work develops a percolation model that describes the drainage of water by oil. This model builds on previous models by utilizing site-bond percolation with independent distributions for pore body and throat size. Additionally, the model can use either effective medium theory (EMT) or critical path theory (CPT) to calculate conductance for media with disordered distribution of bond conductance. It provides a fast and robust computational framework that can be immediately used for intensive pore-scale simulations, which include upscaling for highly heterogeneous pore scale media such as shales, carbonates, and soils. The two methods are compared against a pore network simulator (PNS).

This paper shows that the CPT and EMT techniques show similar relative permeability curves for the invaded phase, but dissimilar results for the invading phase. The results also show that CPT and the PNS show similar permeability curves for the invading phase. Differences between the methods could be the result of boundary conditions, finite network size, and large percolation thresholds.

While we utilize a relatively simple lattice-based pore-network construction approach, the extension to more complex pore networks with highly heterogeneous connections is possible based on pore-network simulations for such media.

This method allows the following conclusions to be drawn:

(1) Critical path theory is superior for calculation of oil relative permeability over effective medium theory in all cases studied.

(2) Effective medium theory shows deviation from pore network simulator close to threshold.

(3) There is no simultaneous two-phase flow at small coordination number. This is due to the high percolation threshold which occurs at small coordination numbers.

(4) There is good agreement between the percolation model and the pore network simulator capillary pressure curves.

(5) Despite the large difference in relative permeability end points, critical path theory shows qualitative agreement with the relative permeability curves generated by the pore network simulator.

ACKNOWLEDGMENTS

This work was supported with supercomputing resources provided by the Phoenix HPC service at the University of Adelaide. This research was supported by Russian Foundation for Basic research (RFBR) and Deutsche Forschungsgemeinschaft (DFG) according to the research Project No. 20-54-12030 (K.M.G.). We thank the two anonymous reviewers for their help in improving the paper.

APPENDIX A: PORE-SCALE CALCULATIONS

1. Calculation of the entry pressure and meniscus curvature

For oil to enter a water wet pore body, or throat, it must displace the water. The interfacial energy between water and a water wet surface will be lower than oil and the water wet surface. The difference in interfacial energy represents the amount of work that must be done for the oil to displace the water. The pressure of the oil phase must be large enough for this work to be done. The pressure at which the oil phase will overcome the work required is called the entry pressure. The entry pressure can be calculated using the MSP Method. The MSP method involves equating the terminal meniscus curvature and the arc meniscus curvature to find the radius at which the displacing phase can enter the pore throat [67].

During piston like displacement, the terminal meniscus curvature is defined by

$$\frac{P_c}{\sigma_{\text{ow}}} = \frac{1}{r_d}, \tag{A1}$$

where P_c is capillary pressure, σ_{ow} is the interfacial tension between oil and water, and r_d is the radius of curvature during drainage. The arc meniscus curvature during piston like displacement and under thermodynamic equilibrium is [68]

$$\frac{P_c}{\sigma_{\text{ow}}} = \frac{L_{\text{ow}} + L_{\text{os}} \cos\theta}{A_{\text{eff}}}, \tag{A2}$$

where L_{ow} is the perimeter of the oil-water contact, L_{os} is the perimeter of the oil-solid contact, θ is contact angle, and A_{eff} is the effective cross-sectional area of the oil. Substitution of (A1) into (A2) results in

$$\frac{1}{r_d} = \frac{L_{\text{ow}} + L_{\text{os}} \cos\theta}{A_{\text{eff}}}. \tag{A3}$$

The cross section of a triangular capillary during MSP displacement is given in Fig. 13.

2. Equations for arbitrary triangular capillaries

The dimensionless shape factor for G is defined as the ratio between the cross sectional area A, and the perimeter L squared [67]:

$$G = \frac{A}{L^2}. \tag{A4}$$

It can be calculated from the relationship between the three half-angles $\beta_i (i = 1, 2, 3)$ which make up the triangle:

$$G = \frac{1}{4\sum_{i=1}^{i=3} \cot \beta_i}. \tag{A5}$$

The perimeter of triangle can be calculated from the inscribed radius r_{in} and the shape factor:

$$L = \frac{r_{\text{in}}}{2G}. \tag{A6}$$

The area of the triangle can also be derived from the inscribed radius and the shape factor:

$$A = \frac{{r_{\text{in}}}^2}{4G}. \tag{A7}$$

During the displacement of water by oil in a triangular capillary, the area and perimeter terms for arbitrary triangles are given by [34]

$$A_{\text{eff}} = A - {r_d}^2 \sum_{i=1}^{i=3} \left[\frac{\cos\theta \cos(\theta + \beta_i)}{\sin \beta_i} + \theta + \beta_i - \frac{\pi}{2} \right], \tag{A8}$$

$$L_{\text{ow}} = 2r_d \sum_{i=1}^{i=3} \left[\frac{\pi}{2} - \beta - \theta \right], \tag{A9}$$

$$L_{\text{os}} = L - 2r_d \sum_{i=1}^{i=3} \left[\frac{\cos(\theta + \beta_i)}{\sin(\beta_i)} \right]. \tag{A10}$$

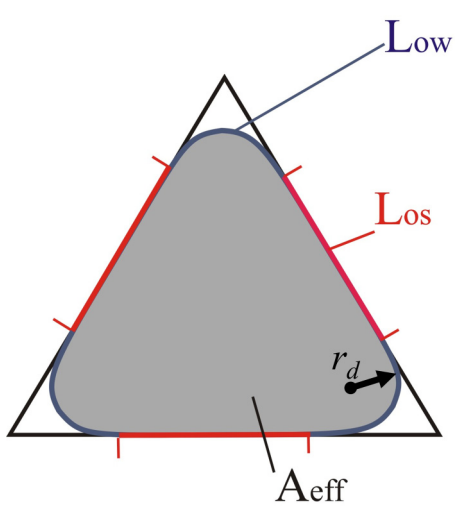

FIG. 13. Cross section of a triangular capillary during Mayer, Stowe, and Princep (MSP) displacement.

After substitution of Eqs. (A4)–(A10) into Eq. (A3), the quadratic solution for r_d is

$$r_d = \frac{r_{\text{in}} \cos\theta (-1 \pm \sqrt{1 + 4GD/\cos^2\theta})}{4GD}, \tag{A11}$$

where D is constant. The equation to calculate D is

$$D = \sum_{i=1}^{i=3} \left[\frac{\cos\theta \cos(\theta + \beta_i)}{\sin \beta_i} + \theta + \beta_i - \frac{\pi}{2} \right] - 2\cos\theta \sum_{i=1}^{i=3} \left[\frac{\cos(\theta + \beta_i)}{\sin(\beta_i)} \right] + 2\sum_{i=1}^{i=3} \left[\frac{\pi}{2} - \beta - \theta \right]. \tag{A12}$$

3. Threshold radius for bonds and sites

Let us assume that all bonds and sites are completely water wet, with $\theta = 0^\circ$. The smallest bond which can be entered by oil will have an inscribed radius which satisfies the following condition:

$$r_b = \frac{\sigma_{\text{ow}}}{P_c D_r}, \tag{A13}$$

where r_b is the inscribed radius of the bond and D_r is a constant. It is derived using MSP theory:

$$D_r = \frac{-1 + \sqrt{1 + 4GD}}{4GD}. \tag{A14}$$

The smallest site which can be entered by oil will have an inscribed radius which satisfies the following condition:

$$r_s > \frac{2\sigma_{\text{ow}}}{P_c}, \tag{A15}$$

where r_s is the inscribed radius of the site.

4. Hydraulic conductance

The flow rate of the oil or water phase through a pore throat or pore body will depend on the shape, cross-sectional area of the phase and the pressure drop. The velocity of each phase is proportional to pressure drop for that phase. The constant of proportionality is called the conductance.

The bonds are modeled as equilateral triangles. The conductance of an equilateral triangle g_b, is given by [69]. Their equation is applied for bond conductance g_b:

$$g_b = 0.6 G_t A^2, \tag{A16}$$

where G_t is the shape factor for a triangle. Sites are modeled as cubes. The conductance of a square is given by [66]. Their equation is applied for the calculation of site conductance g_s:

$$g_s = 0.5623 G_s A^2, \tag{A17}$$

where G_s is the shape factor for a square. The conductance of oil in center of triangle is a simple approximation as given by [34]. Their equation is used for the calculation of conductance to oil in bonds g_{ob}:

$$g_{\text{ob}} = 0.6 G_t A_{\text{eff}}^2. \tag{A18}$$

The conductance of oil in center of square is a simple approximation as given by Ref. [34]. Their equation is used

for the calculation of conductance to oil in sites g_{os}:

$$g_{os} = 0.5623 G_s A_{eff}^2. \tag{A19}$$

During displacement, water will gather in corners. The area of water in each corner A_{wc} can be calculated by

$$A_{wc}(\theta, r_d, \beta) = {r_d}^2\left(\theta + \beta - \frac{\pi}{2} + \frac{\cos\theta\cos(\theta+\beta)}{\sin\beta}\right). \tag{A20}$$

The shape factor for water in the corner G_{wc} is

$$G_{wc}(\theta, r, \beta) = \frac{A_{wc}}{4\left(\frac{r_d\cos(\theta_i+\beta)}{\sin\beta}\right)^2\left(1 - \frac{\sin\beta}{\cos(\theta_i+\beta)}\left(\theta_i + \beta - \frac{\pi}{2}\right)\right)^2}. \tag{A21}$$

Assuming that there is no slip condition at the water-oil boundary, the corner water conductance g_{wc} can then be calculated by [35]:

$$g_{wc} = C A_{wc}^2 G_{wc}, \tag{A22}$$

where the constant C is

$$C = 0.364 + 0.28\frac{\sin\beta\cos\beta}{4G_{wc}(1+\sin\beta)^2}. \tag{A23}$$

To calculate the conductance of the corner water through a site (g_{wcs}) or bond (g_{wcb}), take the corner conductance multiplied by the number of corners. For sites the half-length is $\beta = \pi/4$ and the number of corners is 4. For bonds $\beta = \pi/6$ and the number of corners is 3.

To calculate the conductance from one site to another, we use the equation for a set of conductors in series

$$\frac{l}{g} = \frac{r_{ins1}}{g_{s1}(r_{ins1})} + \frac{l_b}{g_b(r_{inb})} + \frac{r_{ins2}}{g_{s2}(r_{ins2})}, \tag{A24}$$

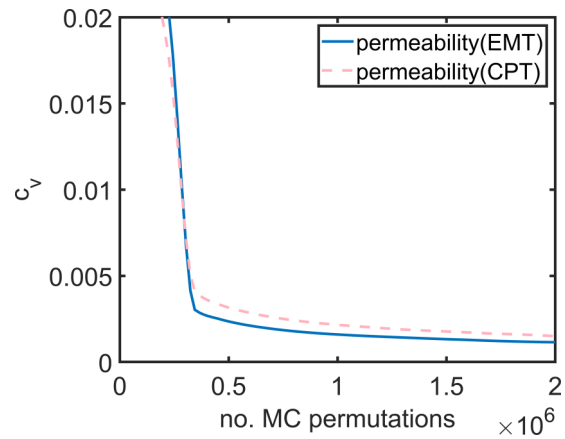

FIG. 14. The coefficient of variation in the permeability calculated by EMT (in red) and by CPT (in blue) plotted against the number of Monte Carlo permutations used to generate the conductance distribution.

where l is the distance between two adjacent site centers, g is the conductance from one site to the other, r_{ins1} and r_{ins2} are the inscribed radius of the first and second site, respectively, g_{s1} and g_{s2} are the conductance for the first and second sites, respectively, g_b is bond conductance, and l_b is the bond length.

The lengths must satisfy the following equation:

$$l_b = l - r_{ins1} - r_{ins2}. \tag{A25}$$

APPENDIX B: CONVERGENCE OF MONTE CARLO SIMULATION

Please see Fig. 14.

[1] M. Sahimi, *Flow and Transport in Porous Media and Fractured Rock: From Classical Methods to Modern Approaches* (Wiley, New York, 2011).

[2] M. J. Blunt, *Multiphase Flow in Permeable Media: A Pore-Scale Perspective* (Cambridge University Press, Cambridge, 2017).

[3] A. Zeinijahromi, T. K. P. Nguyen, and P. Bedrikovetsky, Mathematical model for fines-migration-assisted water flooding with induced formation damage, SPE J. **18**, 518 (2013).

[4] J. R. Godinho, K. M. Gerke, A. G. Stack, and P. D. Lee, The dynamic nature of crystal growth in pores, Sci. Rep. **6**, 33086 (2016).

[5] V. Cnudde and M. N. Boone, High-resolution x-ray computed tomography in geosciences: A review of the current technology and applications, Earth Sci. Rev. **123**, 1 (2013).

[6] P. M. Adler, C. G. Jacquin, and J. A. Quiblier, Flow in simulated porous media, Int. J. Multiph. Flow **16**, 691 (1990).

[7] C. Yeong and S. Torquato, Reconstructing random media. II. Three-dimensional media from two-dimensional cuts, Phys. Rev. E **58**, 224 (1998).

[8] Y. Jiao and N. Chawla, Modeling and characterizing anisotropic inclusion orientation in heterogeneous material via directional cluster functions and stochastic microstructure reconstruction, J. Appl. Phys. **115**, 093511 (2014).

[9] K. M. Gerke, M. V. Karsanina, R. V. Vasilyev, and D. Mallants, Improving pattern reconstruction using directional correlation functions, EPL **106**, 66002 (2014).

[10] J. F. Thovert and P. M. Adler, Grain reconstruction of porous media: Application to a Bentheim sandstone, Phys. Rev. E **83**, 056116 (2011).

[11] P. Tahmasebi and M. Sahimi, Reconstruction of three-dimensional porous media using a single thin section, Phys. Rev. E **85**, 066709 (2012).

[12] H. Li, N. Chawla, and Y. Jiao, Reconstruction of heterogeneous materials via stochastic optimization of limited-angle x-ray tomographic projections, Scr. Mater. **86**, 48 (2014).

[13] H. Li, P. E. Chen, and Y. Jiao, Accurate reconstruction of porous materials via stochastic fusion of limited bimodal microstructural data, Transp. Porous Media **125**, 5 (2017).

[14] S. Khirevich, I. Ginzburg, and U. Tallarek, Coarse-and fine-grid numerical behavior of MRT/TRT lattice-Boltzmann schemes in regular and random sphere packings, J. Comput. Phys. **281**, 708 (2015).

[15] H. Dashtian, S. Bakhshian, S. Hajirezaie, J. P. Nicot, and S. A. Hosseini, Convection-diffusion-reaction of CO_2-enriched brine in porous media: A pore-scale study, Comput. Geosci. **125**, 19 (2019).

[16] A. Q. Raeini, M. J. Blunt, and B. Bijeljic, Modelling two-phase flow in porous media at the pore scale using the volume-of-fluid method, J. Comput. Phys. **231**, 5653 (2012).

[17] C. Bilger, M. Aboukhedr, K. Vogiatzaki, and R. S. Cant, Evaluation of two-phase flow solvers using level set and volume of fluid methods, J. Comput. Phys. **345**, 665 (2017).

[18] D. W. Holmes, J. R. Williams, P. Tilke, and C. R. Leonardi, Characterizing flow in oil reservoir rock using SPH: Absolute permeability, Comput. Part. Mech. **3**, 141 (2016).

[19] V. Shabro, C. Torres-Verdín, F. Javadpour, and K. Sepehrnoori, Finite-difference approximation for fluid-flow simulation and calculation of permeability in porous media, Transp. Porous Media **94**, 775 (2012).

[20] K. M. Gerke, R. V. Vasilyev, S. Khirevich, M. V. Karsanina, D. Collins, T. Sizonenko, D. V. Korost, S. Lamontagne, and D. Mallants, Finite-difference method Stokes solver (FDMSS) for 3D pore geometries: Software development, validation, and case studies, Comput. Geosci. **114**, 41 (2018).

[21] R. Verma, M. Icardi, and M. Prodanović, Effect of wettability on two-phase quasistatic displacement: Validation of two pore scale modeling approaches, J. Contam. Hydrol. **212**, 115 (2018).

[22] F. Frank, C. Liu, A. Scanziani, F. O. Alpak, and B. Riviere, An energy-based equilibrium contact angle boundary condition on jagged surfaces for phase-field methods, J. Colloid Interface Sci. **523**, 282 (2018).

[23] M. R. Rokhforouz and H. A. Akhlaghi Amiri, Phase-field simulation of counter-current spontaneous imbibition in a fractured heterogeneous porous medium, Phys. Fluids **29**, 062104 (2017).

[24] A. Demianov, O. Dinariev, and N. Evseev, Density functional modeling in multiphase compositional hydrodynamics, Can. J. Chem. Eng. **89**, 206 (2011).

[25] K. M. Gerke, M. V. Karsanina, and D. Mallants, Universal stochastic multiscale image fusion: An example application for shale rock, Sci. Rep. **5**, 15880 (2015).

[26] P. Tahmasebi, Nanoscale and multiresolution models for shale samples, Fuel **217**, 218 (2018).

[27] T. Bultreys, L. Van Hoorebeke, and V. Cnudde, Multi-scale, micro-computed tomography-based pore network models to simulate drainage in heterogeneous rocks, Adv. Water Res. **78**, 36 (2015).

[28] M. V. Karsanina, K. M. Gerke, E. B. Skvortsova, A. L. Ivanov, and D. Mallants, Enhancing image resolution of soils by stochastic multiscale image fusion, Geoderma **314**, 138 (2018).

[29] I. Fatt, The network model of porous media I. Capillary pressure characteristics, Petrol. Trans. AIME **207**, 144 (1956).

[30] I. Fatt, The network model of porous media II. Dynamic properties of a single size tube network, Petrol. Trans. AIME **207**, 160 (1956).

[31] I. Fatt, The network model of porous media III. Dynamic properties of networks with tube radius distribution, Petrol. Trans. AIME **207**, 164 (1956).

[32] Q. Xiong, T. Baychev, and A. Jivkov, Review of pore network modeling of porous media: Experimental characterisations, network constructions and applications to reactive transport, J. Contam. Hydrol. **192**, 101 (2016).

[33] J. Gostick, M. Aghighi, J. Hinebaugh, T. Tranter, M. A. Hoeh, H. Day, B. Spellacy, M. H. Sharqawy, A. Bazylak, A. Burns, W. Lehnert, and A. Putz, OpenPNM: A pore network modeling package, Comput. Sci. Eng. **18**, 60 (2016).

[34] P. E. Oren, S. Bakke, and O. J. Arntzen, January. Extending predictive capabilities to network models, in *SPE Annual Technical Conference and Exhibition* (Society of Petroleum Engineers, Richardson, TX, 1997).

[35] P. H. Valvatne and M. J. Blunt, Predictive pore-scale modeling of two-phase flow in mixed wet media, Water Resour. Res. **40**, W07406 (2004).

[36] X. Miao, K. M. Gerke, and T. O. Sizonenko, A new way to parameterize hydraulic conductances of pore elements: A step towards creating pore-networks without pore shape simplifications, Adv. Water Res. **105**, 162 (2017).

[37] A. Q. Raeini, B. Bijeljic, and M. J. Blunt, Generalized network modeling: Network extraction as a coarse-scale discretization of the void space of porous media, Phys. Rev. E **96**, 013312 (2017).

[38] G. G. Pereira, W. V. Pinczewski, D. Y. C. Chan, L. Paterson, and P. E. Øren, Pore-scale network model for drainage-dominated three-phase flow in porous media, Transp. Porous Media **24**, 167 (1996).

[39] M. I. J. Van Dijke and K. S. Sorbie, Pore-scale network model for three-phase flow in mixed-wet porous media, Phys. Rev. E **66**, 046302 (2002).

[40] M. Piri and M. J. Blunt, Three-dimensional mixed-wet random pore-scale network modeling of two-and three-phase flow in porous media. I. Model description, Phys. Rev. E **71**, 026301 (2005).

[41] M. V. Karsanina and K. M. Gerke, Hierarchical Optimization: Fast and Robust Multiscale Stochastic Reconstructions with Rescaled Correlation Functions, Phys. Rev. Lett. **121**, 265501 (2018).

[42] P. E. Chen, W. Xu, N. Chawla, Y. Ren, and Y. Jiao, Hierarchical n-point polytope functions for quantitative representation of complex heterogeneous materials and microstructural evolution, Acta Mater. **179**, 317 (2019).

[43] A. A. Heiba, M. Sahimi, L. E. Scriven, and H. T. Davis, Percolation theory of two-phase relative permeability, SPE Reserv. Eng. **7**, 123 (1992).

[44] R. G. Larson, L. E. Scriven, and H. T. Davis, Percolation theory of two phase flow in porous media, Chem. Eng. Sci. **36**, 57 (1981).

[45] A. A. Heiba, H. T. Davis, and L. E. Scriven, January. Effect of wettability on two-phase relative permeabilities and capillary pressures, in *SPE Annual Technical Conference and Exhibition* (Society of Petroleum Engineers, Richardson, TX, 1983).

[46] M. Blunt, M. J. King, and H. Scher, Simulation and theory of two-phase flow in porous media, Phys. Rev. A **46**, 7680 (1992).

[47] P. Bedrikovetsky and J. Bruining, May. A percolation based upscaling technique for viscous force dominated water flooding in uncorrelated heterogeneous reservoirs, in *IOR 1995–8th European Symposium on Improved Oil Recovery* (European Association of Geoscientists & Engineers, Vienna, Austria, 1995).

[48] P. Bedrikovetsky, *Mathematical Theory of Oil and Gas Recovery (with Applications to ex-USSR Oil and Gas Fields)*, Vol. 4 (Springer Science & Business Media, Berlin, 2013).

[49] V. I. Selyakov and V. Kadet, *Percolation Models for Transport in Porous Media: With Applications to Reservoir Engineering*, Vol. 9 (Springer Science & Business Media, Berlin, 2013).

[50] S. Kirkpatrick, Percolation and conduction, Rev. Mod. Phys. **45**, 574 (1973).

[51] B. Ghanbarian, M. Sahimi, and H. Daigle, Modeling relative permeability of water in soil: Application of effective-medium approximation and percolation theory, Water Resour. Res. **52**, 5025 (2016).

[52] B. Ghanbarian and A. G. Hunt, Improving unsaturated hydraulic conductivity estimation in soils via percolation theory, Geoderma **303**, 9 (2017).

[53] H. Salimi, J. Bruining, and V. Joekar-Niasar, Comparison of modified effective-medium approximation to pore-network theory for relative permeabilities, J. Pet. Sci. Eng. **184**, 106594 (2020).

[54] A. G. Hunt, Applications of percolation theory to porous media with distributed local conductances, Adv. Water Res. **24**, 279 (2001).

[55] V. Ambegaokar, B. I. Halperin, and J. S. Langer, Hopping conductivity in disordered systems, Phys. Rev. B **4**, 2612 (1971).

[56] M. Sahimi, Flow phenomena in rocks: From continuum models to fractals, percolation, cellular automata, and simulated annealing, Rev. Mod. Phys. **65**, 1393 (1993).

[57] S. Galam and A. Mauger, Universal formulas for percolation thresholds. II. Extension to anisotropic and aperiodic lattices, Phys. Rev. E **56**, 322 (1997).

[58] M. Yanuka and R. Englman, Bond-site percolation: Empirical representation of critical probabilities, J. Phys. A **23**, L339 (1990).

[59] K. M. Gerke, T. O. Sizonenko, M. V. Karsanina, E. V. Lavrukhin, V. V. Abashkin, and D. V. Korost, Improving watershed-based pore-network extraction method using maximum inscribed ball pore-body positioning, Adv. Water Res. **140**, 103576 (2020).

[60] K. M. Gerke, M. V. Karsanina, and R. Katsman Calculation of tensorial flow properties on pore level: Exploring the influence of boundary conditions on the permeability of three-dimensional stochastic reconstructions, Phys. Rev. E **100**, 053312 (2019).

[61] V. Joekar-Niasar and S. M. Hassanizadeh, Analysis of fundamentals of two-phase flow in porous media using dynamic pore-network models: A review, Crit. Rev. Environ. Sci. Technol. **42**, 1895 (2012).

[62] T. Bultreys, Q. Lin, Y. Gao, A. Q. Raeini, A. AlRatrout, B. Bijeljic, and M. J. Blunt, Validation of model predictions of pore-scale fluid distributions during two-phase flow, Phys. Rev. E **97**, 053104 (2018).

[63] A. Rabbani, S. Ayatollahi, R. Kharrat, and N. Dashti, Estimation of 3D pore network coordination number of rocks from watershed segmentation of a single 2D image, Adv. Water Res. **94**, 264 (2016).

[64] M. A. Ioannidis, I. Chatzis, and E. A. Sudicky, The effect of spatial correlations on the accessibility characteristics of three-dimensional cubic networks as related to drainage displacements in porous media, Water Resour. Res. **29**, 1777 (1993).

[65] C. E. Diaz, I. Chatzis, and F. A. L. Dullien, Simulation of capillary pressure curves using bond correlated site percolation on a simple cubic network, Transp. Porous Media **2**, 215 (1987).

[66] T. G. Baychev, A. P. Jivkov, A. Rabbani, A. Q. Raeini, Q. Xiong, T. Lowe, and P. J. Withers, Reliability of algorithms interpreting topological and geometric properties of porous media for pore network modeling, Transp. Porous Media **128**, 271 (2019).

[67] G. Mason and N. R. Morrow, Capillary behavior of a perfectly wetting liquid in irregular triangular tubes, J. Colloid Interface Sci. **141**, 262 (1991).

[68] M. Lago and M. Araujo, Threshold pressure in capillaries with polygonal cross section, J. Colloid Interface Sci. **243**, 219 (2001).

[69] T. W. Patzek and D. B. Silin, Shape factor and hydraulic conductance in noncircular capillaries: I. One-phase creeping flow, J. Colloid Interface Sci. **236**, 295 (2001).